

Enhancing the gravitational-wave burst detection confidence in expanded detector networks with the BayesWave pipeline

Yi Shuen C. Lee,^{*} Margaret Millhouse,[†] and Andrew Melatos[‡]

School of Physics, The University of Melbourne, Victoria 3010, Australia

 (Received 23 October 2020; accepted 17 February 2021; published 16 March 2021)

The global gravitational-wave detector network achieves higher detection rates, better parameter estimates, and more accurate sky localization as the number of detectors \mathcal{I} increases. This paper quantifies network performance as a function of \mathcal{I} for *BayesWave*, a source-agnostic, wavelet-based, Bayesian algorithm which distinguishes between true astrophysical signals and instrumental glitches. Detection confidence is quantified using the signal-to-glitch Bayes factor $\mathcal{B}_{S,G}$. An analytic scaling is derived for $\mathcal{B}_{S,G}$ versus \mathcal{I} , the number of wavelets, and the network signal-to-noise ratio SNR_{net} , which is confirmed empirically via injections into detector noise of the Hanford-Livingston (HL), Hanford-Livingston-Virgo (HLV), and Hanford-Livingston-KAGRA-Virgo (HLKV) networks at projected sensitivities for the fourth observing run (O4). The empirical and analytic scalings are consistent; $\mathcal{B}_{S,G}$ increases with \mathcal{I} . The accuracy of waveform reconstruction is quantified using the overlap between injected and recovered waveform, \mathcal{O}_{net} . The HLV and HLKV network recovers 87% and 86% of the injected waveforms with $\mathcal{O}_{\text{net}} > 0.8$, respectively, compared to 81% with the HL network. The accuracy of BayesWave sky localization is ≈ 10 times better for the HLV network than the HL network, as measured by the search area \mathcal{A} , and the sky areas contained within 50% and 90% confidence intervals. Marginal improvement in sky localization is also observed with the addition of the Kamioka Gravitational Wave Detector.

DOI: [10.1103/PhysRevD.103.062002](https://doi.org/10.1103/PhysRevD.103.062002)

I. INTRODUCTION

The Laser Interferometer Gravitational-Wave Observatory (LIGO) [1–3] has completed three observing runs, O1 [4,5], O2 [5,6] and O3 [7] between 2015 and 2020, including joint searches with Italian partner Virgo [8], in the final month of O2 and the whole of O3. In April 2019, Advanced LIGO commenced its third observing run in collaboration with Advanced Virgo as a three-detector network: the Hanford-Livingston-Virgo (HLV) network. The Kamioka Gravitational Wave Detector (KAGRA) [9–11] also began observing in February 2020 [7].

With access to these upgraded instruments, there is a burgeoning interest in detecting short-duration gravitational-wave (GW) signals by combining data from multi-detector networks. These signals typically have durations of milliseconds up to a few seconds, with the most common sources being compact binary coalescences (CBCs) such as black hole or neutron star mergers, along with other potential sources like core-collapse supernovae (SNe) of massive stars [12], pulsar glitches of astrophysical origin [13] and cusps in cosmic strings [14]. In addition to these

known sources, it is also plausible to detect transient signals of unknown astrophysical origin.

Searches for generic GW transients, or burst searches, require the ability to distinguish such signals from any noise artifacts present in the detector data. Hence, it is crucial to understand the noise properties of the detector data. Results from the initial LIGO-Virgo science runs revealed nonstationary and non-Gaussian detector noise, which includes short-duration noise transients denoted by the term “glitches” [15–17]. If not accounted for properly, these features could resemble GWs and consequently limit the ability to detect low-amplitude signals.

Since CBC signals come from known and well-studied sources, such signals are accurately modeled in most regions of parameter space and therefore can be detected with high confidence using matched-filter searches [18–20]. Other GW burst signals, on the other hand, may originate from either complex or unanticipated sources. Given the stochastic nature and complexity of the potential sources (e.g., core collapse supernovae), there are no robust models available to date to assist with the searches of generic burst signals, making it challenging to distinguish them from other non-Gaussian features like glitches in the detector data, as well as to accurately reconstruct the underlying signal waveform.

There are a number of unmodeled burst searches performed in LIGO and Virgo data [21,22]. In this work we look

^{*}ylee9@student.unimelb.edu.au

[†]meg.millhouse@unimelb.edu.au

[‡]amelatos@unimelb.edu.au

at an unmodeled search algorithm called *BayesWave* [23–25], which was proposed to enable the joint detection and characterization of GW bursts and instrumental glitches. BayesWave reconstructs both signals and glitches as a sum of sine-Gaussian wavelets, where the number of wavelets and their parameters are determined via a reversible-jump Markov chain Monte Carlo (RJCMCMC) algorithm. Bayesian model selection is then used to determine the likelihood of an event being a true signal or a noise artifact.

Previous studies have quantified the performance of BayesWave in recovering simulated waveforms from simulated noise with a two-detector network (HL network) [26,27]. However, with Virgo joining GW searches alongside the HL network in O2 and O3, KAGRA coming online toward the end of O3, and future detectors like LIGO-India in the planning stages [28], the network of GW detectors is expanding rapidly. Expanding detector networks will increase the likelihood of detecting more events with higher confidence. These improvements are evident in previous studies and will be elaborated further in Sec. II.

In this paper, we aim to evaluate BayesWave’s performance in searching for GW bursts from detector data beyond the HL network. We achieve this by using BayesWave to recover injected signals from simulated noise with the HLV and the HLKV detector networks and comparing the outcomes with those of the HL network. We quantify the performance of BayesWave based on the following metric: (i) Bayes factor between signal and glitch models, (ii) overlap (match) between injected and recovered waveforms, and (iii) accuracy of recovered sky location. In Sec. III, we provide a detailed overview of the BayesWave algorithm. We derive the analytic scaling relation of the signal-to-glitch Bayes factor in Sec. IV. We then discuss the methods of injecting simulated waveforms into simulated detector noise samples in Sec. V, followed by comparisons and analyses of the metrics mentioned above: Bayes factor in Sec. VI A, overlap in Sec. VI B and sky localization in Sec. VI C. Finally, we present a summary of the results along with their implications in Sec. VII.

II. BENEFITS OF EXPANDING DETECTOR NETWORKS

Increasing the number of operational ground-based detectors has several major benefits for GW astronomy, including a higher rate of detection of GW transients and better characterization of those signals. Here we discuss some of the benefits of adding new detectors to the existing network.

A. SNR and search volume

One major advantage of a larger detector network is the ability to confidently detect quieter events. The strain amplitude $s^{(i)}$ in detector i of the network consists of a

signal $h^{(i)}$ (if present) and detector noise $n^{(i)}$ which can be expressed as

$$s^{(i)} = h^{(i)} + n^{(i)}. \quad (1)$$

The squared matched-filter signal-to-noise ratio (SNR) of signal $h_s^{(i)}$ in detector i is then given by [29]

$$\text{SNR}_i^2 = (h_s^{(i)} | h_s^{(i)}), \quad (2)$$

where $(\cdot | \cdot)$ on the right-hand side of the expression is the noise-weighted inner product. We define the noise-weighted inner product between two arbitrary waveforms $h_a(t)$ and $h_b(t)$ as [30]

$$(h_a | h_b) = \int_0^\infty \frac{\tilde{h}_a^*(f) \tilde{h}_b(f) + \tilde{h}_a(f) \tilde{h}_b^*(f)}{S_n(f)} df, \quad (3)$$

where $\tilde{h}(f)$ is the Fourier-transformed waveform, $\tilde{h}^*(f)$ is its complex conjugate and $S_n(f)$ is the one-sided power spectral density (PSD) of stationary, Gaussian detector noise.

For a network with \mathcal{I} detectors, the overall network SNR is given by [26]

$$\text{SNR}_{\text{net}}^2 = \sum_{i=1}^{\mathcal{I}} \text{SNR}_i^2. \quad (4)$$

According to Eq. (4), adding more detectors to the network increases the SNR of all detected GW signals. This enables detection pipelines to estimate waveform parameters more accurately [31]. With improved parameter estimates, more accurate models can be constructed to represent the detected waveform [32].

In addition, the SNR of GW signals scales with luminosity distance D_L as [33]

$$\text{SNR}_i \propto \frac{1}{D_L}. \quad (5)$$

By combining Eqs. (4) and (5) and assuming coherent searches, the overall SNR for a network of \mathcal{I} detectors with equal sensitivities is given by $\text{SNR}_{\text{net}} \propto \sqrt{\mathcal{I}}/D_L$. Assuming that GW sources are uniformly distributed across the sky, an \mathcal{I} -detector network can detect $\sqrt{\mathcal{I}}$ times further and up to $\sqrt{\mathcal{I}}^3$ more sources compared to a single-detector network since the search volume scales as $V \propto D_L^3$.

B. Sky coverage

The sensitivity of a detector toward a particular sky location is determined by the antenna pattern in that given direction. Adding more detectors to the network at different geographical locations and orientations increases the

sensitivity of the network to a wider region of the sky (increased sky coverage), consequently increasing the detection rate and volume along those directions [34].

Reference [35] presented a visual comparison between the network antenna pattern across the whole sky between a three-detector (HLV) network and a four-detector (HLKV) network, where “K” denotes KAGRA. As expected, results show that both networks are more sensitive to some regions in the sky than others. However, the HLKV network has a higher overall network antenna power pattern and an overall increase in sky coverage is also reflected in the expansion of regions with relatively higher sensitivity.

C. Observing time

Adding detectors to the existing network also increases the duty cycle where two or more detectors are functional and simultaneously observing. This consequently increases the chances of the detectors picking up a coherent astrophysical signal and leading to higher detection rates [34].

D. Sky localization

Sky localization of a GW source is of vital importance for locating and identifying any existing electromagnetic counterparts to the GW event [36]. Ground-based GW detectors are nearly omnidirectional, so with a single detector we are not able to impose a strict constraints to the sky location of a GW event. Nevertheless, sky localization of GW signals improves significantly with multiple interferometers. The times of arrival at two detectors constrain the position of the source to an error ellipse in the sky map. Thus, having more detectors will reduce localization volume by imposing stricter constraints to the location of the sources, improving the accuracy of locating the source in the sky [36,37].

To sum up the points above, the advantages of having more detectors in the network include (i) improvement in SNR and increased search volume, (ii) alignment-dependent sky coverage, (iii) increased rates of detection, and (iv) improved sky localization.

III. BAYESWAVE OVERVIEW

BayesWave is a Bayesian data analysis algorithm that detects transient features in a stretch of detector data and identifies whether they are an astrophysical signal or instrumental noise. BayesWave reconstructs non-Gaussian features in the data using a sum of sine-Gaussian (also called Morlet-Gabor) wavelets. The number of wavelets and their respective parameters are sampled using a transdimensional Markov chain Monte Carlo algorithm, otherwise known as the RJMCMC. The RJMCMC is implemented to allow for adjustable number of wavelets and hence variable model dimensions. BayesWave outputs posterior distributions and Bayesian evidences for three separate models: (i) Gaussian noise

only, (ii) Gaussian noise with glitches and (iii) Gaussian noise with GW signal. The model evidences are then used for Bayesian model selection between the three scenarios.

A. Wavelet frames

BayesWave uses a sum of sine-Gaussian (also called Morlet-Gabor) wavelets to reconstruct non-Gaussian features (either signals or glitches) in the detector data. Even though sine-Gaussian wavelets form a nonorthogonal frames,¹ their shape is variable in the time-frequency plane and can optimally reconstruct a transient GW signal with no *a priori* assumption on the signal source or morphology.

The number of wavelets used in the reconstruction is marginalized via the RJMCMC, where signals with complex structure in the time-frequency plane will use more wavelets in the reconstruction. Previous studies [26,38] have shown that the number of wavelets scales linearly with SNR such that

$$N \approx \gamma + \beta \text{SNR}, \quad (6)$$

where γ and β are constants which depend on waveform morphology. The results from Ref. [26] show that β and hence N increase with waveform complexity. For binary black hole (BBH) waveforms, the typical numbers are $\gamma = 5.6$ and $\beta = 0.066$ for sine-Gaussian wavelet reconstructions [38].

In BayesWave, each wavelet in the time domain has five intrinsic parameters t_0 , f_0 , Q , A , and ϕ_0 which represent central time, central frequency, quality factor, amplitude and phase offset, respectively. These intrinsic parameters can be expressed as a single parameter vector $\lambda = \{t_0, f_0, Q, A, \phi_0\}$ and the mathematical representation of a sine-Gaussian wavelet is given by

$$\Psi(t; t_0, f_0, Q, A, \phi_0) = A e^{-\Delta t^2/\tau^2} \cos(2\pi f_0 \Delta t + \phi_0) \quad (7)$$

with $\tau = Q/(2\pi f_0)$ and $\Delta t = t - t_0$ [26].

The glitch model in BayesWave is independent between detectors owing to the fact that noise artifacts are uncorrelated across different detectors. Hence, the set of glitch model parameters must contain the respective parameters for each individual detector across the network. The complete set of glitch model parameters for a network of detectors comprising Hanford, Livingston, and Virgo (HLV) can be written as [26]

¹Discrete wavelets can form orthogonal bases for signal or glitch representations, but projecting the signal wavelets onto each detector requires the time translation operator which is computationally expensive. Despite the lack of orthogonality, sine-Gaussian wavelets are flexible in shape and have an analytic Fourier representation. Hence the analysis can be done in the frequency domain without the need of a time-translation operator. Further details can be found in Sec. 3 of [24].

$$\theta_{\mathcal{G}} = \{\lambda^H \cup \lambda^L \cup \lambda^V\} \quad (8)$$

with $\lambda^i = \{\lambda_0^i \cup \lambda_1^i \cup \dots \cup \lambda_{N_{\mathcal{G}}^i}^i\}$, where the numerical subscripts indicate a single wavelet used in the glitch model and $N_{\mathcal{G}}$ is the total number of wavelets in the glitch model. The superscripts indicates the i th detector in the network.

In contrast to the glitch model, the signal model is common across all detectors in the network. As a result, signal models should have a single set of intrinsic wavelet parameters $\lambda^{\oplus} = \{\lambda_0 \cup \lambda_1 \cup \dots \cup \lambda_{N_s}\}$, along with a set of extrinsic parameter $\Omega = \{\alpha, \delta, \psi, \epsilon\}$ which sequentially describes the right ascension (RA), declination (dec), polarization angle and ellipticity of the GW signal. The sky location (RA, dec) and polarization angle of a source determine antenna beam patterns of the detector network, as well as provide information on the amplitude and the arrival-time delay of the signal in each detector [39]. Ellipticity defines the relative phase and amplitude of the plus and cross polarizations, h_+ and h_{\times} , respectively, with $h_{\times} = \epsilon h_+ e^{i\pi/2}$. The ellipticity parameter ϵ takes values between 0 and 1 with the lower and upper bounds denoting linear to circular polarizations, respectively [24]. Altogether a complete set of signal model parameters is given by [26]

$$\theta_{\mathcal{S}} = \{\lambda^{\oplus} \cup \Omega\}. \quad (9)$$

BayesWave produces posterior distributions of the parameters described above. Each draw from the posterior contains a unique set of wavelet parameters (and extrinsic parameters for the signal model), which are then summed to produce a posterior on the waveform, $h(t)$. By using this basis of sine-Gaussian wavelets, $h(t)$ is reconstructed with *no a priori* assumption on the source of the GW signal.

B. Model selection

In addition to waveform reconstruction, BayesWave performs model selection between the signal and glitch hypotheses described above. The ratio of model evidences, otherwise known as the Bayes factor, is the key to model selection in Bayesian inference as it assesses the plausibility of two different models, \mathcal{M}_{α} and \mathcal{M}_{β} , parameterized by their respective parameter sets $\vec{\theta}_{\alpha}$ and $\vec{\theta}_{\beta}$. In other words, it quantifies which model is better supported by the data. The model evidence (also called the marginalized evidence) is given by

$$p(\vec{s}|\mathcal{M}_{\alpha}) = \int p(\vec{\theta}_{\alpha}|\mathcal{M}_{\alpha})p(\vec{s}|\vec{\theta}_{\alpha}, \mathcal{M}_{\alpha})d\vec{\theta}_{\alpha}, \quad (10)$$

where \vec{s} is the observed data, \mathcal{M}_{α} is the model, and $\vec{\theta}_{\alpha}$ is the parameter vector for model \mathcal{M}_{α} . The prior probability of parameters $\vec{\theta}_{\alpha}$ before the data are observed is given by

$p(\vec{\theta}_{\alpha}|\mathcal{M}_{\alpha})$, and $p(\vec{s}|\vec{\theta}_{\alpha}, \mathcal{M}_{\alpha})$ is the likelihood of obtaining the observed data \vec{s} , given the model \mathcal{M}_{α} . Hence, the Bayes factor between models \mathcal{M}_{α} and \mathcal{M}_{β} , parameterized by their respective parameter vectors $\vec{\theta}_{\alpha}$ and $\vec{\theta}_{\beta}$, is

$$\mathcal{B}_{\alpha,\beta}(\vec{s}) = \frac{p(\vec{s}|\mathcal{M}_{\alpha})}{p(\vec{s}|\mathcal{M}_{\beta})}. \quad (11)$$

$\mathcal{B}_{\alpha,\beta}(\vec{s}) > 1$ implies that model \mathcal{M}_{α} is more strongly supported by the data than model \mathcal{M}_{β} . To reduce computational costs, the BayesWave algorithm calculates model evidence using thermodynamic integration [40].

BayesWave calculates the Bayes factor between the signal model (i.e., the data contain a real astrophysical signal) and the glitch model (i.e., the data contain an instrumental glitch). In Sec. IV we discuss how the signal-to-glitch Bayes factor scales with SNR, the number of wavelets used in the MCMC, and the number of detectors in the network.

C. Overlap

In addition to distinguishing between signals and glitches, BayesWave also produces a posterior distribution of the wavelet-expanded waveforms, $h(t)$, to match the true waveform, $h_s(t)$. One way to quantify the agreement or similarity between $h(t)$ and $h_s(t)$ is through the overlap \mathcal{O} . Reconstructed waveforms in BayesWave are analogous to waveform templates; hence, the overlap between reconstructed models and the injected waveform can be computed the same way as the overlap in matched filtering.

The normalized overlap between the two waveforms can be written as [32]

$$\mathcal{O} = \frac{(h|h_s)}{\sqrt{(h|h)(h_s|h_s)}}, \quad (12)$$

where $(\cdot|\cdot)$ is the noise-weighted inner product as defined in Eq. (3). Since Eq. (12) is normalized, \mathcal{O} takes values between -1 and 1 . When $\mathcal{O} = 1$, there is a perfect match between the injected and recovered waveform; $\mathcal{O} = 0$ implies that there is no match at all and $\mathcal{O} = -1$ implies a perfect anticorrelation.

Equation (12) only applies to a single detector. A network overlap \mathcal{O}_{net} is required to fully evaluate BayesWave's performance in recovering waveforms from all the detectors combined. In order to define the network overlap, we sum each factor in Eq. (12) over all \mathcal{I} detectors in the network such that

$$\mathcal{O}_{\text{net}} = \frac{\sum_{i=1}^{\mathcal{I}} (h^{(i)}|h_s^{(i)})}{\sqrt{\sum_{i=1}^{\mathcal{I}} (h^{(i)}|h^{(i)}) \sum_{i=1}^{\mathcal{I}} (h_s^{(i)}|h_s^{(i)})}}, \quad (13)$$

where $h^{(i)}$ and $h_s^{(i)}$ denote the recovered waveform and waveform present in detector i , respectively.

IV. ANALYTIC BAYES FACTOR SCALING

In this work, we aim to understand the behavior of the Bayes factor between signal and glitch models for networks comprising different numbers of GW detectors. Hence it is in our interest to analytically understand the conditions of model selection. We want to know under what circumstances a model is favored over another.

A. Occam penalty

A key to understanding Bayes factor behavior when using a transdimensional model, as BayesWave does, is the role of the Occam penalty.

The parameter value at which the posterior distribution peaks is known as the maximum *a posteriori* (MAP) value, denoted as $\vec{\theta}_{\text{MAP}}$. For high SNR events, the integrand of model evidence in Eq. (10) peaks sharply in the vicinity of the MAP. Following the Laplace-Fisher approximation, the integral can be estimated as

$$p(\vec{s}|\mathcal{M}) \simeq p(\vec{s}|\vec{\theta}_{\text{MAP}}, \mathcal{M}) p(\vec{\theta}_{\text{MAP}}|\mathcal{M}) (2\pi)^{D/2} \sqrt{\det C}, \quad (14)$$

where $p(\vec{s}|\vec{\theta}_{\text{MAP}}, \mathcal{M})$ is the MAP likelihood; $p(\vec{\theta}_{\text{MAP}}|\mathcal{M})$ is the prior evaluated at the MAP parameter values; D is the dimension of the model; and $\det C$ is the determinant of the full covariance matrix for the N wavelets used in waveform reconstruction. If the covariance matrix for a single wavelet is C_n , then we have

$$\det C = \prod_{n=1}^N \det C_n, \quad (15)$$

assuming minimal overlap between the wavelet parameter spaces. Since the Laplace-Fisher approximation is associated with the MAP likelihood, the covariance matrix can be approximated as the inverse of the Fisher information matrix (FIM), Γ [41]. A comprehensive discussion of the FIM and its relation to wavelet parameter jump proposal is presented in Appendix A.

By definition, $\det C$ measures the variance of the likelihood. Thus, $\sqrt{\det C}$ quantifies the characteristic spread of the likelihood function. The product of $\sqrt{\det C}$ and $(2\pi)^{D/2}$, which account for the dimensionality of the model, can then be used as a measure for the volume of the uncertainty ellipsoid (posterior volume), $\Delta V_{\mathcal{M}}$ for a given model \mathcal{M} [26,42,43]. Assuming uniform priors for all wavelet parameters, one can also write $p(\vec{\theta}_{\text{MAP}}|\mathcal{M}) = 1/V_{\mathcal{M}}$, where $V_{\mathcal{M}}$ represents the total parameter space volume. Hence, the last three factors of Eq. (14) can collectively be interpreted as the fraction of the prior occupied by the posterior distribution, such that the model evidence is now given by

$$p(\vec{s}|\mathcal{M}) \simeq p(\vec{s}|\vec{\theta}_{\text{MAP}}, \mathcal{M}) \frac{\Delta V_{\mathcal{M}}}{V_{\mathcal{M}}}, \quad (16)$$

where $\Delta V_{\mathcal{M}}/V_{\mathcal{M}}$ is the ‘‘Occam penalty factor.’’

Following Eqs. (11) and (16), the Bayes factor between two models can be reexpressed as

$$\mathcal{B}_{\alpha,\beta}(\vec{s}) = \Lambda_{\alpha,\beta}(\vec{s}) \frac{\Delta V_{\alpha} V_{\beta}}{V_{\alpha} \Delta V_{\beta}}, \quad (17)$$

where the ratio of MAP likelihoods is given by

$$\Lambda_{\alpha,\beta}(\vec{s}) = \frac{p(\vec{s}|\vec{\theta}_{\text{MAP},\alpha})}{p(\vec{s}|\vec{\theta}_{\text{MAP},\beta})}. \quad (18)$$

Equation (17) suggests that the Bayes factor is dependent on the likelihood ratio and the ratio of the Occam penalty factors. The Occam factor penalizes models that require an unnecessarily large parameter space volume to fit the data by suppressing the model evidence. Note that the Occam penalty is not an intentionally added component to the Bayes factor; rather, it is inherently imposed as a result of using the Bayes theorem.

As a heuristic explanation as to how the Occam penalty aids in BayesWave’s ability to distinguish between signals and glitches, recall that signal models (\mathcal{S}) for each detector share the same intrinsic parameters and four extrinsic parameters. Since there are five intrinsic parameters (t_0 , f_0 , Q , A , and ϕ_0) per wavelet, the dimension of signal models scales as

$$D_{\mathcal{S}} \sim 5N + 4, \quad (19)$$

where N is the number of wavelets. Glitch models (\mathcal{G}), on the other hand, have no extrinsic parameters but the glitch model of each detector is described by a unique set of intrinsic parameters. Assuming that signal and glitch models use the same number of wavelets such that $N^{\mathcal{G}} = N^{\mathcal{S}} = N$ (see Appendix B), the dimension of glitch models scales as [24]

$$D_{\mathcal{G}} \sim 5NI. \quad (20)$$

One therefore has $D_{\mathcal{G}} > D_{\mathcal{S}}$ for $\mathcal{I} \geq 2$. This implies that the total parameter space volume for the glitch model is larger than that of the signal model (i.e., $V_{\mathcal{G}} > V_{\mathcal{S}}$). If both models fit the data equally well (i.e., $\Lambda_{\mathcal{S},\mathcal{G}} \approx 1$ and $\Delta V_{\mathcal{S}} \approx V_{\mathcal{G}}$), then by Occam’s razor we should expect to see a selection bias toward the signal model as \mathcal{I} increases. In other words, Eq. (17) gives

$$\mathcal{B}_{\mathcal{S},\mathcal{G}}(\vec{s}) = \Lambda_{\mathcal{S},\mathcal{G}}(\vec{s}) \frac{\Delta V_{\mathcal{S}} V_{\mathcal{G}}}{\Delta V_{\mathcal{G}} V_{\mathcal{S}}} > 1 \quad (21)$$

with increasing \mathcal{I} .

In Sec. IV B, we use the Laplace approximation to the Bayesian evidence to derive an analytic scaling of the Bayes factor.

B. Dependence of Bayes factor on number of detectors

In Ref. [26], Littenberg *et al.* put forth an analytic scaling of the log signal-to-glitch Bayes factor, $\ln \mathcal{B}_{S,G}$, in an effort to fully understand BayesWave's ability to robustly distinguish astrophysical signals from instrumental glitches. They showed that the primary scaling of the Bayes factor goes as

$$\ln \mathcal{B}_{S,G} \propto N \ln(\text{SNR}_{\text{net}}), \quad (22)$$

where N is the number of wavelets used in the reconstruction, which is related to the signal morphology and SNR as described in Eq. (6). The dependence of Bayes factor on N (and therefore the complexity of the signal in the time frequency plane) differentiates BayesWave from other unmodeled searches whose detection statistics scale primarily with SNR. The scaling found in Ref. [26] assumes a network comprising two GW detectors. Here we extend this work to an arbitrary number of detectors \mathcal{I} .

We begin with the Laplace approximation of model evidences for the signal and glitch models. From Eq. (14), we find

$$\begin{aligned} \ln p(d|S) \simeq & \frac{\text{SNR}_{\text{net}}^2}{2} - \frac{5N^S}{2} - N^S \ln(V_\lambda) \\ & + \sum_{n=1}^{N^S} \ln\left(\frac{\bar{Q}_n}{\text{SNR}_{\text{net},n}^5}\right) + \frac{D_\Omega}{2} + \ln \frac{\sqrt{\det C_\Omega}}{V_\Omega}, \end{aligned} \quad (23)$$

$$\begin{aligned} \ln p(d|G) \simeq & \frac{\text{SNR}_{\text{net}}^2}{2} - \sum_{i=1}^{\mathcal{I}} \left[\frac{5N_i^G}{2} + N_i^G \ln(V_\lambda) \right. \\ & \left. - \sum_{n=1}^{N_i^G} \ln\left(\frac{\bar{Q}_n}{\text{SNR}_{i,n}^5}\right) \right] \end{aligned} \quad (24)$$

with $\bar{Q}_n \equiv (2\pi)^{5/2} \frac{\sqrt{2}Q_n}{\pi}$. V_λ is the prior volume of intrinsic parameters and N_i^x is the total number of wavelets for model x . The subscript i refers to detector i in the network and n labels an individual wavelet from the set of wavelets for a given model. For instance, $\text{SNR}_{i,n}$ is the SNR of wavelet n in the i th detector.² In the last two terms of Eq. (23), $D_\Omega = 4$, C_Ω and V_Ω denote the dimension, covariance matrix and the prior volume of extrinsic parameters, respectively. The full derivation from Eq. (14) to Eqs. (23) and (24) can be found in Sec. III (A) of Ref. [26].

²Each individual wavelet used in signal or glitch model reconstruction has an amplitude which can be converted into to SNR. For details, see [24].

To simplify the expressions for these evidences, we follow the same assumptions used in Ref. [26] and which are detailed further in Appendix B. One simplifying assumption we highlight here again is that the number of wavelets used in the signal model will be approximately the same as the glitch model, and so we set $N^S = N^G \equiv N$ [i.e., the N in Eq. (22)]. Upon implementing the assumptions in Appendix B, the theoretical log Bayes factor between the signal and glitch model for a network of \mathcal{I} detector(s) is given by $\ln \mathcal{B}_{S,G} \simeq \ln p(d|S) - \ln p(d|G)$:

$$\begin{aligned} \ln \mathcal{B}_{S,G} \simeq & (\mathcal{I} - 1) \left[\frac{5N}{2} + N \ln(V_\lambda) - \sum_{n=1}^N \ln(\bar{Q}_n) \right. \\ & \left. + 5N \ln\left(\frac{\text{SNR}_{\text{net}}}{\sqrt{N}}\right) \right] - \frac{5}{2} \mathcal{I} N \ln(\mathcal{I}) \\ & + \left(2 + \ln \frac{\sqrt{\det C_\Omega}}{V_\Omega} \right). \end{aligned} \quad (25)$$

The equation shows explicit dependence of the Bayes factor on network SNR, number of wavelets and number of detectors. We pay close attention to the scaling

$$\ln \mathcal{B}_{S,G} \propto \mathcal{I} N \ln \text{SNR}_{\text{net}} \quad (26)$$

which now has an extra scaling factor of \mathcal{I} compared to Eq. (22).

The dependence on the number of wavelets used implies that the signal model is favored over the glitch model with increasing waveform complexity (higher N). In other words, a more complex waveform is more likely to be classified as a signal [26]. This analytic result agrees with the discussion in Sec. IV A where if two models fit the data equally well, the less complex model will be selected to represent the waveform. The proportionality $\ln \mathcal{B}_{S,G} \propto \mathcal{I}$ suggests that for signals with equal SNR and N , the Bayes factor should increase if we increase the number of detectors in the network. Again, this result agrees with the discussion in Sec. IV A; including more detectors in the network increases the dimensionality of the glitch model and thus the signal model will be even more strongly preferred.

V. INJECTION DATASET

To empirically test the Bayes factor scaling given by Eq. (25), as well as investigate the effect on waveform reconstructions with detector networks of different sizes, we inject a set of simulated BBH signals into simulated detector noise and recover them using BayesWave. While BayesWave is a flexible algorithm that can detect a variety of signals from different sources, we use BBH waveforms as our test bed because they are well-understood sources and have previously been used to study the performance of BayesWave [26,32,44].

In this work, we use tools from the LIGO Analysis Library [45] to inject a set of nonspinning BBHs with equal

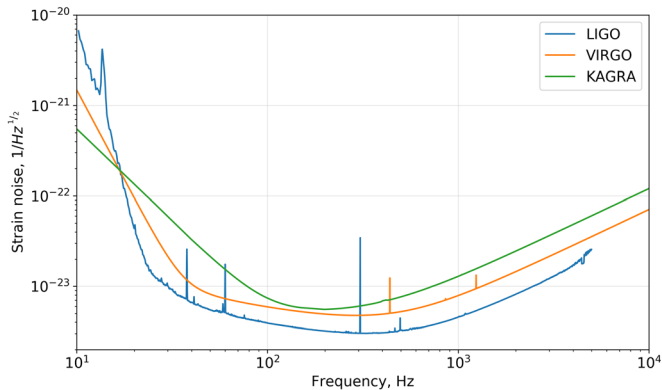


FIG. 1. Projected LIGO, Virgo and KAGRA strain noise (i.e., amplitude spectral density), $\sqrt{S_n}$ as a function of frequency for the fourth observing run O4. The data used to generate the noise curves above are retrieved from [48].

component masses of $30 M_\odot$. We use the phenomenological waveform IMRPhenomD to model spinning but non-precessing binaries using a combination of analytic post-Newtonian, effective-one-body and numerical relativity methods [46,47]. The GW sources are distributed isotropically across the sky, and the inclinations i are distributed uniformly in $\arccos i$. SNR_{net} is distributed uniformly in $\text{SNR}_{\text{net}} \in \{10, 50\}$ where this SNR is calculated from a network comprising the HL detectors.

We inject 150 BBH signals into Gaussian noise colored by the projected PSD of LIGO, Virgo and KAGRA for the fourth observing run O4, as given in the LIGO, Virgo and KAGRA observing scenario [48]. The noise curves are shown in Fig. 1.

We then recover the injected signals with BayesWave in three different scenarios: (i) running only on Hanford and Livingston (HL) data (a two-detector network), (ii) running on the Hanford, Livingston, and Virgo (HLV) data (a three-detector network) and (iii) running on the Hanford, Livingston, KAGRA and Virgo (HLKV) data (a four-detector network). All three detector configurations use the exact same injection dataset.

In the two following sections, Secs. VI A and VI B, we analyze two figures of merit: (i) Bayes factor and (ii) the overlap. By comparing these quantities between the HL and HLV networks, we can evaluate the performance of BayesWave in recovering the injected waveforms from detector networks of different sizes. As an extension to previous studies on sky localization with expanded detector networks, we also compare the accuracy of BayesWave in recovering the sky location from detector networks of different sizes in Sec. VI C.

VI. RESULTS

A. Recovered Bayes factors

After analyzing the injections described in Sec. V, we use the model evidences calculated by BayesWave to

understand the impact of GW detector network size on the log signal-to-glitch Bayes factor $\ln \mathcal{B}_{S,G}$. For all the analyses in this paper, we use only injections that have been identified as inconsistent with Gaussian noise (this can be either a signal or glitch) by BayesWave. Injections indicated to be consistent with the Gaussian noise model (\mathcal{N}) by BayesWave are removed from the dataset, since it would be meaningless to evaluate their respective signal and glitch model evidences. In other words, injections with $\ln \mathcal{B}_{S,\mathcal{N}}$ error bars encompassing values below zero are removed from the dataset. The widths of $\ln \mathcal{B}_{S,\mathcal{N}}$ error bars are given by [24]

$$\Delta[\ln \mathcal{B}_{S,\mathcal{N}}] = \sqrt{\{\Delta[\ln p(d|\mathcal{S})]\}^2 + \{\Delta[\ln p(d|\mathcal{N})]\}^2}, \quad (27)$$

where $\Delta[\ln p(d|\mathcal{M})]$ is the uncertainty for the logarithmic evidence of model \mathcal{M} . A total of 14 data points are removed under this constraint. These events are all low SNR_{net} injections.

The top left panel of Fig. 2 shows $\ln \mathcal{B}_{S,G}$ as a function of SNR_{net} for the HL, HLV and HLKV networks. All three networks show a clear trend of increasing Bayes factor with increasing network SNR as expected. Our results also show that the HLKV injections have the highest SNR overall, agreeing with Eq. (4) which indicates that increasing \mathcal{I} increases SNR_{net} . Furthermore, we can see that injections at comparable SNRs are recovered with higher $\ln \mathcal{B}_{S,G}$ in the HLV network than the HL network. In other words, even after accounting for the increased SNR, we observe further enhancement in detection confidence for an expanded detector network, suggesting that $\ln \mathcal{B}_{S,G}$ is related to \mathcal{I} , and not just the SNR of the signal as predicted by Eq. (25).

The top right panel of Fig. 2 shows the median number of wavelets used in the BayesWave reconstruction, N versus the injected SNR in the respective detector networks, SNR_{net} . The median here refers to the median of posterior distribution for N . We see that N increases systematically with SNR_{net} in both the HL and HLV networks. This is expected since the detectors are able to pick up more complex features of the waveform at high SNR. At low SNR ($\text{SNR} \lesssim 15$) there is a slight deviation from the linear trend described by Eq. (6) between N and SNR in both detector networks. This is primarily due to the prior on the number of wavelets. This prior is determined empirically from runs in LIGO data after O1 and peaks around $N = 3$ [25]. N also depends on waveform morphology and complexity [26,38]. Injecting the same set of BBH waveforms into all three detector configurations results in similar trends between N and SNR_{net} .

Equation (25) shows that $\ln \mathcal{B}_{S,G}$ also scales with the number of wavelets used in the reconstruction. Hence we also show empirically how the dimensionality of signal model (i.e., the number of wavelets) also contributes to the increase in $\ln \mathcal{B}_{S,G}$ for different \mathcal{I} . We show this in the bottom panel of Fig. 2 by plotting $\ln \mathcal{B}_{S,G}$ versus N . Color

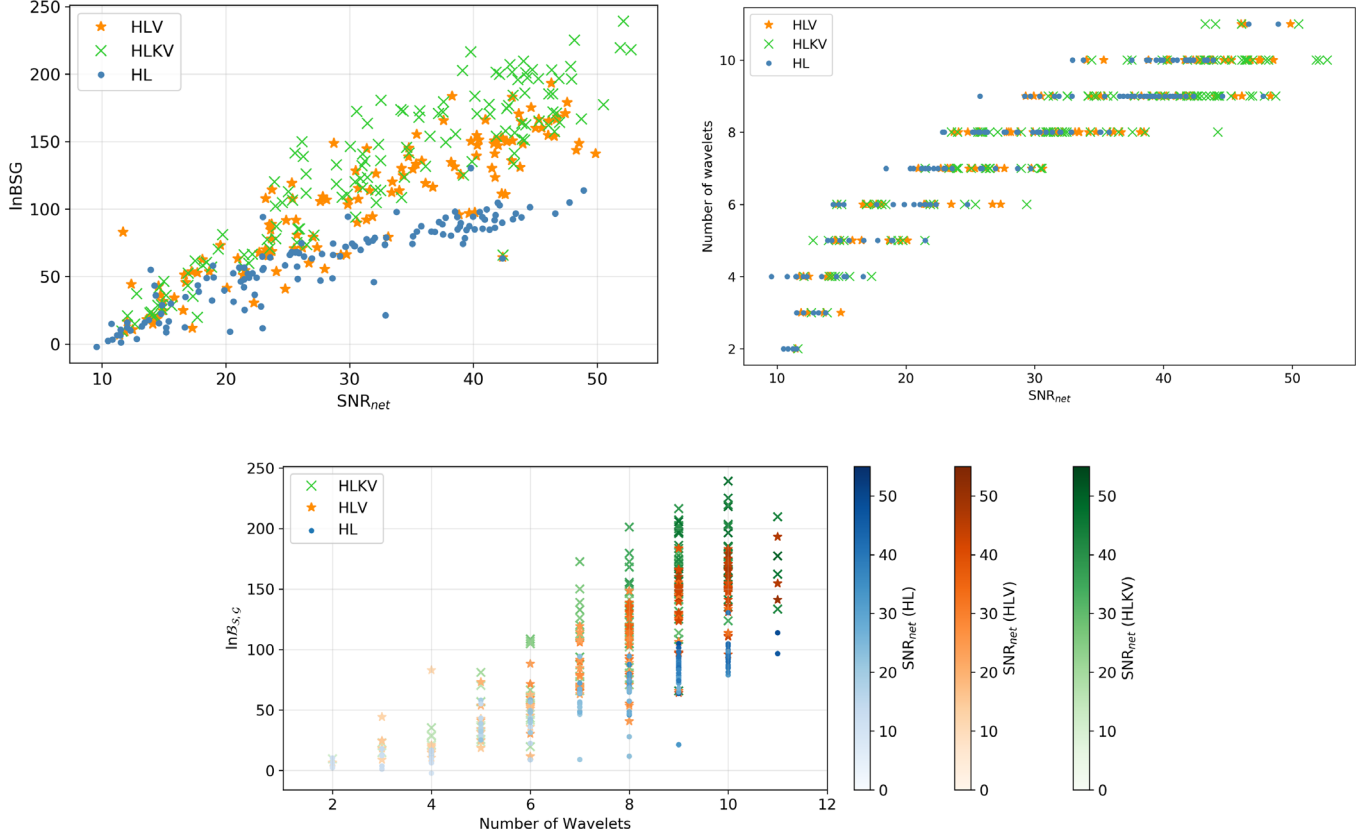


FIG. 2. The top left panel shows the log signal-to-glitch Bayes factor $\ln \mathcal{B}_{S,G}$ of BBH injection recoveries versus network signal-to-noise ratio SNR_{net} . Each data point represents one BBH injection. The top right panel shows the median number of wavelets used in signal model reconstruction for each injection, N versus SNR_{net} . The bottom panel shows $\ln \mathcal{B}_{S,G}$ versus N , and the three color bars indicate the network SNR of each data point in the corresponding detector network. In the top panels, the horizontal axis corresponds three different network SNRs: (i) For the blue dot data points it corresponds to SNR_{net} of the HL network, (ii) for the orange star data points it corresponds to SNR_{net} of the HLV network, and (iii) for the green cross data points it corresponds to SNR_{net} of the HLKV network.

bars indicate the SNR_{net} of each data point. For all three detector configurations, $\ln \mathcal{B}_{S,G}$ generally increases with N , as predicted by Eq. (25). At low SNRs (i.e., $\text{SNR} < 15$), detector networks recover the waveform with $N \leq 3$ and $\ln \mathcal{B}_{S,G} \leq 50$ because low SNR injections have low-amplitude features which are harder to reconstruct resulting in lower detection confidence. It is clear for injections recovered with $N > 3$ that $\ln \mathcal{B}_{S,G}$ in the HLKV network are generally higher than that of the HL and HLV networks at comparable N and SNR_{net} . This again emphasizes the point that the Bayes factor scales with \mathcal{I} .

A more thorough investigation of the relation between the empirical and analytic Bayes factor can be found in Appendix C, where we use a simplified injection set of single sine-Gaussian wavelets. By recovering sine-Gaussian wavelets with sine-Gaussian wavelets, Eq. (6) reduces to $N = 1$. The results show that the empirical scaling of the Bayes factor with \mathcal{I} agrees with the analytical scaling in Eq. (25) to a good approximation.

In summary, we show by comparing Bayes factors between the HL, HLV and HLKV networks that expanding detector networks increases detection confidence. Our empirical

results are consistent with the analytic results discussed Sec. IV, viz. $\ln \mathcal{B}_{S,G} \propto \mathcal{I} N \ln \text{SNR}_{\text{net}}$. Heuristically, this can be understood via Occam's razor: if coincident identical

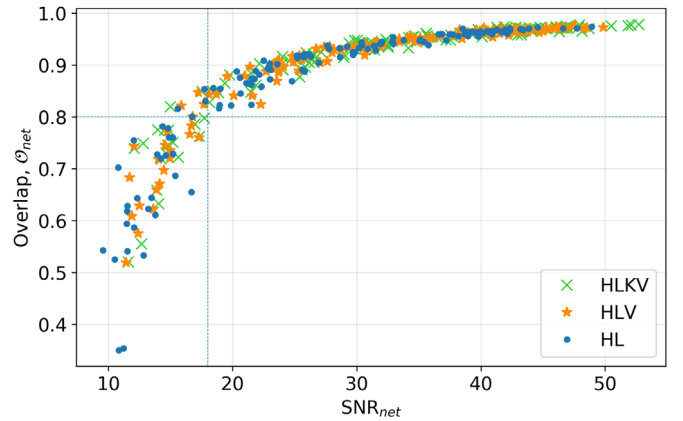


FIG. 3. Median overlap between the injected and recovered waveform \mathcal{O}_{net} of the HL (blue dot) and HLV (orange star) network, as a function of SNR_{net} . The horizontal blue line indicates $\mathcal{O}_{\text{net}} = 0.8$ and the vertical blue line indicates $\text{SNR}_{\text{net}} > 15$.

glitches are unlikely in two detectors, they are even more unlikely in three or more detectors. Therefore when identical waveforms are detected simultaneously across larger networks, they have a higher likelihood of being a signal.

B. Recovered waveform overlap

In the previous section, we showed that for a set of BBH waveforms $\ln \mathcal{B}_{S,g}$ increases with a larger number of detectors in the network, meaning with more detectors our confidence in detection is strengthened. In this section, we quantify the accuracy of BayesWave in waveform

recovery by comparing the overlap (also sometimes called the match) between the injected and recovered waveforms for the HL, HLV and HLKV detector networks. The network overlap \mathcal{O}_{net} is given by Eq. (13). For the rest of this paper, any mention of overlap refers to the network overlap.

Figure 3 shows the median overlap \mathcal{O}_{net} as a function of network SNR, where \mathcal{O}_{net} of all three detector networks show positive correlation with their respective network SNR. This observation is consistent with previous results, which show that network overlap scales with SNR [38,44]. To illustrate how waveform reconstruction improves with

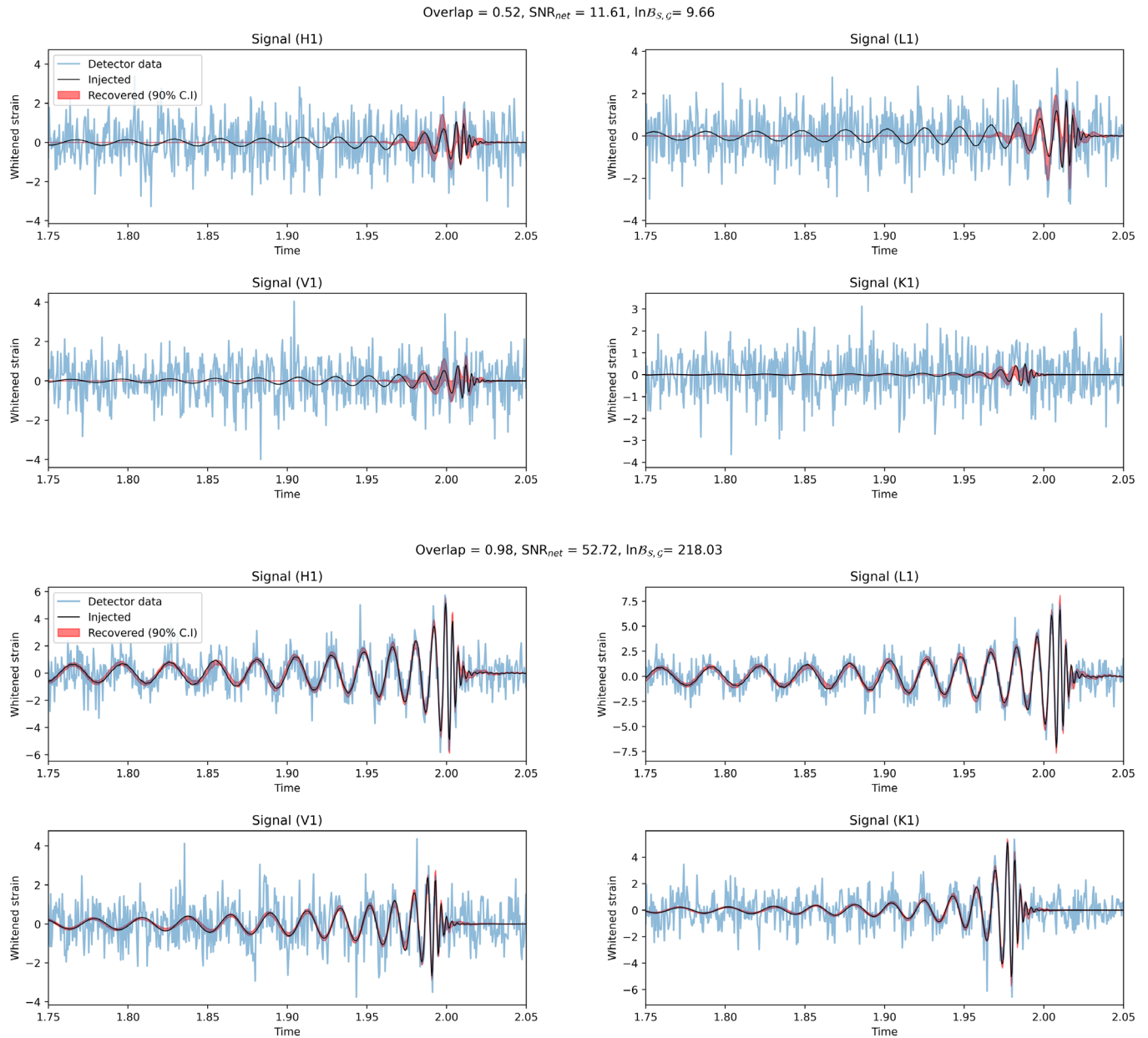


FIG. 4. The top panel shows, for an injection with $\text{SNR}_{\text{net}} = 11.61$ and $\mathcal{O} = 0.52$, the injected waveform (black line), the detector data (blue line) and the 90% credible interval of the recovered waveform (red line) for each detector in the HLKV network. Similarly in the bottom panel but for an injection with $\text{SNR}_{\text{net}} = 52.72$ and $\mathcal{O} = 0.98$.

SNR, Fig. 4 shows the injected waveform (black line), the detector data (blue line) and the 90% credible interval of the recovered waveform (red line) for two events in the HLKV network. The top and bottom panels show the waveforms for the injection recovered with the smallest overlap ($\mathcal{O}_{\min} = 0.52$) and largest overlap ($\mathcal{O}_{\max} = 0.98$) of the whole injection dataset, respectively. The event with the smallest overlap has $\text{SNR}_{\text{net}} = 11.6$ and was recovered with $\ln \mathcal{B}_{S,G} = 9.66$, while the event with the largest overlap has $\text{SNR}_{\text{net}} = 52.72$ and was recovered with $\ln \mathcal{B}_{S,G} = 218.0$. This is consistent with the observed trend between overlap and network SNR in Fig. 3. The similar trend between overlap and network SNR between all three detector configurations indicates that waveform reconstruction fidelity is not directly related to the number of detectors in the network.

However, as noted earlier, increasing the number of detectors does increase the network SNR. By comparing the percentage of waveforms recovered with overlap above a given threshold for all three detector configurations, we show that having an additional detector allows us to better reconstruct the signal waveform. The threshold is arbitrarily defined here to be $\mathcal{O}_{\text{net}} > 0.8$ and is indicated by the horizontal blue line in Fig. 3. We found that 81% of the injections were recovered with $\mathcal{O}_{\text{net}} > 0.8$ for the HL network, 86% for the HLV network and 87% for the HLKV network.

While the inclusion of additional detector(s) does not have an extra benefit in the same way it does for the Bayes factor as shown in the previous section, it nonetheless allows us to better reconstruct the signal waveform due to increased SNR. However, the improvement is less significant upon the addition of KAGRA, since it is less sensitive compared to Virgo as shown in Fig. 1 and therefore the increase in SNR is less compared to when Virgo is added to the network. The overall results also show that BayesWave is able to reconstruct waveforms reasonably well with all three detector configurations for injections with $\text{SNR}_{\text{net}} > 18$ as indicated by the vertical blue line in Fig. 3.

C. Sky localization

Expanding detector networks improves sky localization of GW events, as has been shown by various studies on coherent network detections e.g., [34,36,49]; see Sec. II. In this section, we compare the accuracy of BayesWave in locating the source with the HL and HLV networks. We use two separate measures: (i) sky area enclosed within the 50% and 90% credible intervals (CI) and (ii) search area \mathcal{A} .

For every injection, BayesWave produces posterior distributions for the sky location (in the form of right ascension and declination) of the GW signal. We first look at the sky area enclosed within 50% and 90% credible intervals (CIs) of the posterior distribution of source location. In the left panel of Fig. 5, we show the plot for sky area enclosed within the 50% CI versus network SNR for each injection, and similarly for the 90% CI on the right panel. For all three detector configurations, we note that the area within the 50% and 90% CIs measured in square degrees (deg^2) fundamentally reduces with increasing network SNR due to improved accuracy in arrival time differences [36]. However, both sky areas are generally an order of magnitude smaller for the HLV network compared to the HL network. Upon addition of the KAGRA detector, we observe further reduction in the sky area, but not as drastic as that between the HL and HLV networks since KAGRA is less sensitive than Virgo. The areas enclosed within both 50% and 90% CIs reduces with increasing \mathcal{I} due to the additional arrival time differences which further constrain the location of each source. These results reiterate that accuracy of sky localization improves at fixed CI as \mathcal{I} increases.

We also compare the inferred sky location with the true injected location of the source. We introduce another metric—the search area \mathcal{A} , the hypothetical sky area observed by a detector before it correctly points toward the true location. To define this quantity mathematically, we first denote the posterior probability density function (PDF) of sky location as $p_{\text{sky}}(\phi, \theta)$. If the true location of the source

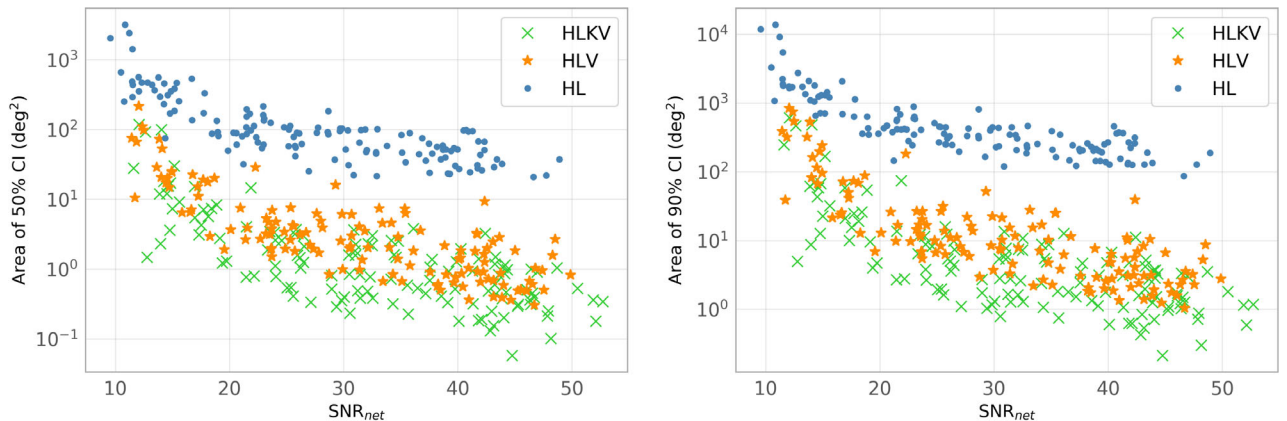


FIG. 5. The left panel shows the sky area enclosed within the 50% credible interval (CI) in square degrees versus the network SNR of the corresponding detector network. Similarly on the right panel, except for the 90% CI.

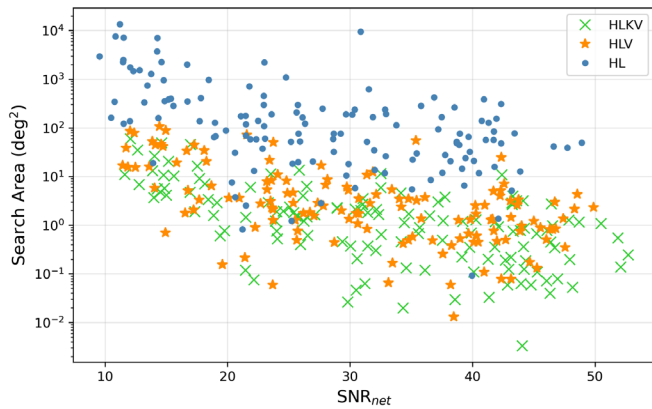


FIG. 6. Search area \mathcal{A} [Eq. (28)] versus network SNR for the HL (blue dots) and HLV (orange stars) networks.

is (ϕ_t, θ_t) and $p_0 = p_{\text{sky}}(\phi_t, \theta_t)$, then all points within \mathcal{A} should have $p_{\text{sky}} \geq p_0$. Mathematically, we write [32,50]

$$\mathcal{A} = \int H[p_{\text{sky}}(\phi, \theta) - p_0] d\Omega, \quad (28)$$

where H is the Heaviside step function and $d\Omega$ is the surface area element on the celestial sphere, i.e., $d\Omega = \cos \delta d\theta d\phi$. In Fig. 6 we plot the search area \mathcal{A} against network SNR for both the HL and HLV networks. The HLKV search area is slightly smaller than the HLV search area, which in turn is significantly smaller than the HL search area, consistent with Fig. 5.

Overall, we see that sky localization improves remarkably when a detector of high sensitivity is added to the network. If a less sensitive detector is added, the improvements are small but not negligible.

VII. CONCLUSION

The aim of this study is to compare the performance of BayesWave in recovering GW waveforms from detector networks of different sizes. We derive an analytic scaling for the Bayes factor between the signal and glitch models, $\mathcal{B}_{S,G}$. We then inject a set of simulated BBH signals of fixed masses at different SNRs into simulated O4 detector data of the HL, HLV and HLKV network. We quantify BayesWave’s performance in signal identification with $\mathcal{B}_{S,G}$ and the performance in waveform reconstruction with overlap \mathcal{O}_{net} . We also compare the accuracy of sky localization between the two networks.

We find that events of similar injected SNR analyzed using the HLV and HLKV network have higher $\ln \mathcal{B}_{S,G}$ than those using the HL network. This agrees with theoretical prediction of the Bayes factor scaling:

$$\ln \mathcal{B}_{S,G} \propto \mathcal{I} N \ln \text{SNR}_{\text{net}}. \quad (29)$$

Previous work [26] demonstrated that BayesWave is unique among GW unmodeled burst searches in that the so-called

“complexity” of the signal in the time-frequency plane plays a crucial role in the detection statistic, rather than just the signal’s strength. This is understood through the factor of N in Eq. (29): a signal with more complex structure needs more wavelets to accurately reconstruct the waveform. In this work, we expose another novel feature of the BayesWave algorithm: the detection statistic is also influenced by the number of detectors, i.e., the factor of \mathcal{I} in Eq. (29). Events of similar injected SNR (SNR_{net}) analyzed using larger detector networks have higher $\ln \mathcal{B}_{S,G}$, indicating detection confidence increases more than we would expect purely from the increase in SNR_{net} .

The network overlap \mathcal{O}_{net} between the injected and recovered waveforms increases with SNR_{net} . We also show that 87% of the HLKV network, 86% of the HLV network and 81% of the HL network injections have $\mathcal{O} > 0.8$. Since larger detector networks can detect signals at higher SNR, they pick up more details of the true waveform. Thus, BayesWave can reconstruct the waveforms more accurately.

Finally, in Sec. VI C, we quantify accuracy of sky localization with the sky area enclosed within the 50% and 90% CI. We find that both areas decrease with increasing SNR_{net} and are generally an order of magnitude smaller for the HLV networks than the HL network. The reduction of sky area is less significant upon the addition of the KAGRA detector due to its low sensitivity compared to Virgo. The search area \mathcal{A} also decreases with increasing SNR_{net} and increasing number of detectors. The overall results suggest that increasing the number of detectors at different geographical locations improves sky localization, consistent with previous analyses [34,36,49].

With the global detector network growing in size, the outlook for improving detection confidence with unmodeled burst searches is promising. Prospective work along the lines of the research presented in this paper may include injecting different waveform morphologies to compare detection confidence between detector networks of different sizes. We also recommend looking into quantifying and comparing the outcomes of BayesWave in recovering simulated signals from more realistic detector noise (i.e., in the presence of glitches) between different detector configurations.

In summary, BayesWave shows significant improvements in terms of waveform recovery and parameter estimation when working with a larger detector network. This promising result suggests that, with more detectors joining the global network in the future, we will be able to reconstruct generic GW burst signals more accurately using BayesWave making detections with higher Bayes factor and hence with higher confidence.

ACKNOWLEDGMENTS

Parts of this research were conducted by the Australian Research Council Centre of Excellence for

Gravitational Wave Discovery (OzGrav), through Project No. CE170100004. The authors are grateful for computational resources provided by the LIGO Laboratory and supported by National Science Foundation Grants No. PHY-0757058 and No. PHY-0823459. We thank Bence Bécsey for his helpful comments.

APPENDIX A: FISHER INFORMATION MATRIX

Each wavelet has its Fisher information matrices (FIMs), Γ written in terms of its five intrinsic parameters $\{t_0, f_0, Q, \ln A, \phi_0\}$:

$$\Gamma = \text{SNR}^2 \begin{pmatrix} \frac{4\pi^2 f_0^2 (1+Q^2)}{Q^2} & 0 & 0 & 0 & -2\pi f_0 \\ 0 & \frac{3+Q^2}{4f_0^2} & -\frac{3}{4Qf_0} & -\frac{1}{2f_0} & 0 \\ 0 & -\frac{3}{4Qf_0} & \frac{3}{4Q^2} & \frac{1}{2Q} & 0 \\ 0 & -\frac{1}{2f_0} & \frac{1}{2Q} & 1 & 0 \\ -2\pi f_0 & 0 & 0 & 0 & 1 \end{pmatrix}. \quad (\text{A1})$$

FIMs contain information on local curvature of the likelihood of wavelet parameters which accelerates convergence by proposing jumps in the MCMC algorithm toward regions of higher likelihood [24]. BayesWave uses FIMs to update wavelet parameters by drawing proposals from a multivariate Gaussian distribution

$$q(\mathbf{y}|\mathbf{x}) = \frac{\det \Gamma}{(2\pi)^2} \exp\left(-\frac{1}{2} \Gamma_{ij} \Delta x^i \Delta x^j\right), \quad (\text{A2})$$

where $\Delta x^i = x^i - y^i$ denotes the displacement in intrinsic parameter i before and after the update.

APPENDIX B: ASSUMPTIONS FOR BAYES FACTOR SCALING

Laplace approximations for the logarithmic signal (\mathcal{S}) and glitch (\mathcal{G}) model evidences are given by Eqs. (23) and (24), respectively. In order to see how $\mathcal{B}_{\mathcal{S},\mathcal{G}}$ scales with the waveform parameters, we make some assumptions to simplify the two logarithmic evidences. In this work we use the same assumptions as in Ref. [26].

Loud signals typically have optimal extrinsic parameters across the detector network, so the SNR in each detector will be approximately equal such that

$$\text{SNR}_{i,n} \approx \frac{\text{SNR}_{\text{net},n}}{\sqrt{\mathcal{I}}}, \quad (\text{B1})$$

where $\text{SNR}_{i,n}$ is the SNR of the n th wavelet in detector i . We use a further simplifying assumption that the SNR of each wavelet is the same

$$\text{SNR}_{\text{net},n} \approx \frac{\text{SNR}_{\text{net}}}{\sqrt{N}}, \quad (\text{B2})$$

which has been empirically validated. We assume that the glitch model in each detector uses similar reconstruction parameters as the signal model, and as such the quality factors of all wavelets are approximately equal:

$$Q_{i,n}^{\mathcal{G}} \approx Q_n^{\mathcal{S}} \equiv Q \quad (\text{B3})$$

and, similarly,

$$N^{\mathcal{G}} \approx N^{\mathcal{S}} \equiv N. \quad (\text{B4})$$

Recall that $N^{\mathcal{G}}$ indicates the number of wavelets used in the glitch model for a *single* detector, so for an \mathcal{I} -detector network, the total number of wavelets used in glitch models across the entire network is $\mathcal{I}N$.

Equations (23) and (24) can be simplified to

$$\begin{aligned} \ln p(d|\mathcal{S}) &\simeq \frac{\text{SNR}_{\text{net}}^2}{2} - \frac{5N}{2} - N \ln(V_\lambda) \\ &\quad + \sum_{n=1}^N \ln(\bar{Q}_n) - 5N \ln\left(\frac{\text{SNR}_{\text{net}}}{\sqrt{N}}\right) \\ &\quad + \left(2 + \ln \frac{\sqrt{\det C_\Omega}}{V_\Omega}\right), \end{aligned} \quad (\text{B5})$$

$$\begin{aligned} \ln p(d|\mathcal{G}) &\simeq \frac{\text{SNR}_{\text{net}}^2}{2} - \mathcal{I} \left[\frac{5N}{2} + N \ln(V_\lambda) \right. \\ &\quad \left. - \sum_{n=1}^N \ln(\bar{Q}_n) + 5N \ln\left(\frac{\text{SNR}_{\text{net}}}{\sqrt{N\mathcal{I}}}\right) \right]. \end{aligned} \quad (\text{B6})$$

APPENDIX C: SCALING OF BAYES FACTOR WITH \mathcal{I}

Our results in Sec. VI A show that $\ln \mathcal{B}_{\mathcal{S},\mathcal{G}}$ scales with SNR, N , and \mathcal{I} . As per Eq. (6), N itself depends on both the SNR of the signal and the waveform morphology. In order to specifically test the scaling of $\ln \mathcal{B}_{\mathcal{S},\mathcal{G}}$ with \mathcal{I} alone, we inject a set of sine-Gaussian wavelets as coherent signals into detector noise for the HL, HLV and HLKV network and then recover them using BayesWave. Because sine-Gaussian wavelets are the basis of reconstruction for BayesWave, the number of wavelets used is $N = 1$, with no dependence on SNR.

The dataset used this analysis is a set of 150 single sine-Gaussian wavelets. The parameters of each wavelet are randomly drawn from the following distributions: $t_0 \in [1.5, 2.5]$ s (where $t = 1$ s is the center of the analysis window), $f_0 \in [32, 1000]$ Hz, $Q \in [0.1, 40]$ and $\phi_0 \in [0, 2\pi]$. The SNR of the signals are drawn randomly from a uniform distribution and $\text{SNR} \in [10, 50]$, and the amplitude is then found, viz.

$$A = \text{SNR} \sqrt{\frac{2\sqrt{2\pi}f_0 S_n(f_0)}{Q}} \quad (\text{C1})$$

(see [38] for details). As we are injecting a coherent signal, we also require four extrinsic parameters as described in Sec. III A. These parameters are also drawn randomly from uniform distributions such that $\alpha \in [0, 2\pi]$, $\delta \in [-\pi/2, \pi/2]$, $\psi \in [0, 2\pi]$ and $\epsilon \in [-0.99, 0.99]$.

In Fig. 7, we plot $\ln \mathcal{B}_{S,G}$ of each injection against SNR_{net} for the HL, HLV and HLKV network injections. We note that $\ln \mathcal{B}_{S,G}$ increases with SNR_{net} and is generally higher for networks with greater \mathcal{I} , as predicted from Eq. (26). Since N in this case does not depend on SNR, we can be certain that the differences in $\ln \mathcal{B}_{S,G}$ between the different detector configurations at comparable SNR_{net} are entirely due to \mathcal{I} .

In order to compare the analytic and empirical scaling of $\ln \mathcal{B}_{S,G}$ with \mathcal{I} , we fit analytic approximation of $\ln \mathcal{B}_{S,G}$ for each detector network with a generalized expression

$$\ln \mathcal{B}_{S,G} \approx (\mathcal{I} - 1)[5 \ln \text{SNR}_{\text{net}} + a] + \frac{5}{2} \mathcal{I} \ln \mathcal{I} + b. \quad (\text{C2})$$

This expression is derived from Eq. (25) with $N = 1$. We define the constants $a = \frac{5}{2} - \ln(V_\lambda) + \ln(Q)$ and $b = 2 + \ln \frac{\det C_\Omega}{V_\Omega}$. The prior volumes V_λ and V_Ω are, respectively, the same for all detector configurations. We do not have an analytic expression for $\det C_\Omega$ as the FIM approximation is inadequate; the extrinsic parameter space contains degeneracy between parameters, resulting in

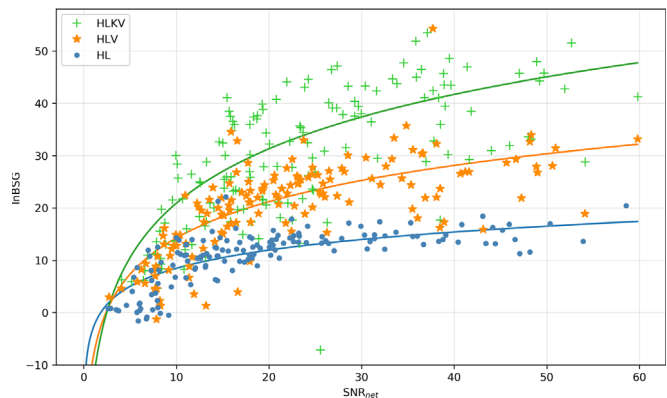


FIG. 7. Log signal-to-glitch Bayes factor $\ln \mathcal{B}_{S,G}$ of sine-Gaussian wavelet recoveries versus network signal-to-noise ratio SNR_{net} . The solid lines with colors corresponding to the data symbols are analytic predictions of $\ln \mathcal{B}_{S,G}$ given by Eq. (C2).

multimodal, non-Gaussian likelihood distribution which spans the full extent of the prior range (see [26] for details). We present the fits as three solid lines in Fig. 7, where we have determined by eye $a = -10$ and $b = 4$. The same values of a and b are used for all three fits and they are broadly consistent with the empirical results.

We see general agreement between the empirical results and predicted scaling for $\ln \mathcal{B}_{S,G}$, which further confirms our results in Sec. VI A that the Bayes factor does not only depend on SNR_{net} but also on \mathcal{I} . We again note that these scalings are estimations, and due to the different sensitivities of the detectors we do not expect exact agreement between analytic prediction and empirical results.

-
- [1] J. Aasi, B. P. Abbott, R. Abbott, T. Abbott *et al.*, Advanced LIGO, *Classical Quantum Gravity* **32**, 074001 (2015).
 - [2] B. P. Abbott, R. Abbott, R. Adhikari, P. Ajith *et al.*, LIGO: The laser interferometer gravitational-wave observatory, *Rep. Prog. Phys.* **72**, 076901 (2009).
 - [3] G. M. Harry, Advanced LIGO: The next generation of gravitational wave detectors, *Classical Quantum Gravity* **27**, 084006 (2010).
 - [4] B. P. Abbott, R. Abbott, T. D. Abbott *et al.*, All-sky search for short gravitational-wave bursts in the first Advanced LIGO run, *Phys. Rev. D* **95**, 042003 (2017).
 - [5] B. P. Abbott, R. Abbott, T. D. Abbott *et al.*, GWTC-1: A Gravitational-Wave Transient Catalog of Compact Binary Mergers Observed by LIGO and Virgo during the First and Second Observing Runs, *Phys. Rev. X* **9**, 031040 (2019).
 - [6] B. P. Abbott, R. Abbott, T. D. Abbott *et al.*, All-sky search for short gravitational-wave bursts in the second Advanced LIGO and Advanced Virgo run, *Phys. Rev. D* **100**, 024017 (2019).
 - [7] I. Georgescu, O3 highlights, *Nat. Rev. Phys.* **2**, 222 (2020).
 - [8] F. Acernese, M. Agathos, K. Agatsuma, D. Aisa, N. Allemandou *et al.*, Advanced Virgo: A second-generation interferometric gravitational wave detector, *Classical Quantum Gravity* **32**, 024001 (2015).
 - [9] T. Akutsu, M. Ando, K. Arai *et al.*, First cryogenic test operation of underground km-scale gravitational-wave observatory KAGRA, *Classical Quantum Gravity* **36**, 165008 (2019).
 - [10] T. Akutsu, M. Ando, K. Arai, Y. Arai *et al.*, Overview of KAGRA: Detector design and construction history, *arXiv:2005.05574*.
 - [11] Y. Aso, Y. Michimura, K. Somiya, M. Ando, O. Miyakawa, T. Sekiguchi, D. Tatsumi, and H. Yamamoto, Interferometer design of the KAGRA gravitational wave detector, *Phys. Rev. D* **88**, 043007 (2013).
 - [12] C. L. Fryer and K. C. B. New, Gravitational waves from gravitational collapse, *Living Rev. Relativity* **14**, 1 (2011).

- [13] E. Stopnitzky and S. Profumo, Gravitational waves from gamma-ray pulsar glitches, *Astrophys. J.* **787**, 114 (2014).
- [14] T. Damour and A. Vilenkin, Gravitational radiation from cosmic (super)strings: Bursts, stochastic background, and observational windows, *Phys. Rev. D* **71**, 063510 (2005).
- [15] L. Blackburn, L. Cadonati, S. Caride, S. Caudill, S. Chatterji *et al.*, The LSC glitch group: Monitoring noise transients during the fifth LIGO science run, *Classical Quantum Gravity* **25**, 184004 (2008).
- [16] J. Aasi, J. Abadie, B. P. Abbott, R. Abbott, T. Abbott *et al.*, Characterization of the LIGO detectors during their sixth science run, *Classical Quantum Gravity* **32**, 115012 (2015).
- [17] J. Aasi, J. Abadie, B. P. Abbott, R. Abbott, T. D. Abbott *et al.*, The characterization of Virgo data and its impact on gravitational-wave searches, *Classical Quantum Gravity* **29**, 155002 (2012).
- [18] S. A. Usman, A. H. Nitz, I. W. Harry *et al.*, The PyCBC search for gravitational waves from compact binary coalescence, *Classical Quantum Gravity* **33**, 215004 (2016).
- [19] S. Sachdev, S. Caudill, H. Fong *et al.*, The GstLAL search analysis methods for compact binary mergers in Advanced LIGO's second and Advanced Virgo's first observing runs, [arXiv:1901.08580](https://arxiv.org/abs/1901.08580).
- [20] S. Hooper, S. K. Chung, J. Luan, D. Blair, Y. Chen, and L. Wen, Summed parallel infinite impulse response filters for low-latency detection of chirping gravitational waves, *Phys. Rev. D* **86**, 024012 (2012).
- [21] R. Lynch, S. Vitale, R. Essick, E. Katsavounidis, and F. Robinet, Information-theoretic approach to the gravitational-wave burst detection problem, *Phys. Rev. D* **95**, 104046 (2017).
- [22] S. Klimenko, I. Yakushin, A. Mercer, and G. Mitselmakher, A coherent method for detection of gravitational wave bursts, *Classical Quantum Gravity* **25**, 114029 (2008).
- [23] T. B. Littenberg and N. J. Cornish, Bayesian inference for spectral estimation of gravitational wave detector noise, *Phys. Rev. D* **91**, 084034 (2015).
- [24] N. J. Cornish and T. B. Littenberg, Bayeswave: Bayesian inference for gravitational wave bursts and instrument glitches, *Classical Quantum Gravity* **32**, 135012 (2015).
- [25] N. J. Cornish, T. B. Littenberg, B. Bécsy, K. Chatziioannou, J. A. Clark, S. Ghonge, and M. Millhouse, BayesWave analysis pipeline in the era of gravitational wave observations, *Phys. Rev. D* **103**, 044006 (2021).
- [26] T. B. Littenberg, J. B. Kanner, N. J. Cornish, and M. Millhouse, Enabling high confidence detections of gravitational-wave bursts, *Phys. Rev. D* **94**, 044050 (2016).
- [27] J. B. Kanner, T. B. Littenberg, N. Cornish, M. Millhouse, E. Xhakaj, F. Salemi, M. Drago, G. Vedovato, and S. Klimenko, Leveraging waveform complexity for confident detection of gravitational waves, *Phys. Rev. D* **93**, 022002 (2016).
- [28] C. S. Unnikrishnan, IndIGO and Ligo-India scope and plans for gravitational wave research and precision metrology in India, *Int. J. Mod. Phys. D* **22**, 1341010 (2013).
- [29] C. Cutler and É. E. Flanagan, Gravitational waves from merging compact binaries: How accurately can one extract the binary's parameters from the inspiral waveform?, *Phys. Rev. D* **49**, 2658 (1994).
- [30] D. G. Keppel, Signatures and dynamics of compact binary coalescences and a search in LIGO's S5 data, PhD thesis, California Institute of Technology, 2009.
- [31] S. M. Gaebel and J. Veitch, How would GW150914 look with future gravitational wave detector networks?, *Classical Quantum Gravity* **34**, 174003 (2017).
- [32] B. Bécsy, P. Raffai, N. J. Cornish, R. Essick, J. Kanner, E. Katsavounidis, T. B. Littenberg, M. Millhouse, and S. Vitale, Parameter estimation for gravitational-wave bursts with the BayesWave pipeline, *Astrophys. J.* **839**, 15 (2017).
- [33] H.-Y. Chen and D. E. Holz, The loudest gravitational wave events, [arXiv:1409.0522](https://arxiv.org/abs/1409.0522).
- [34] B. F. Schutz, Networks of gravitational wave detectors and three figures of merit, *Classical Quantum Gravity* **28**, 125023 (2011).
- [35] A. Manzotti and A. Dietz, Prospects for early localization of gravitational-wave signals from compact binary coalescences with advanced detectors, [arXiv:1202.4031](https://arxiv.org/abs/1202.4031).
- [36] C. Pankow, E. A. Chase, S. Coughlin, M. Zevin, and V. Kalogera, Improvements in gravitational-wave sky localization with expanded networks of interferometers, *Astrophys. J.* **854**, L25 (2018).
- [37] W. Del Pozzo, C. P. L. Berry, A. Ghosh, T. S. F. Haines, L. P. Singer, and A. Vecchio, Dirichlet process Gaussian-mixture model: An application to localizing coalescing binary neutron stars with gravitational-wave observations, *Mon. Not. R. Astron. Soc.* **479**, 601 (2018).
- [38] M. Millhouse, N. J. Cornish, and T. Littenberg, Bayesian reconstruction of gravitational wave bursts using chirplets, *Phys. Rev. D* **97**, 104057 (2018).
- [39] J. B. Camp and N. J. Cornish, Gravitational wave astronomy, *Annu. Rev. Nucl. Part. Sci.* **54**, 525 (2004).
- [40] T. B. Littenberg and N. J. Cornish, Bayesian approach to the detection problem in gravitational wave astronomy, *Phys. Rev. D* **80**, 063007 (2009).
- [41] M. Abt and W. J. Welch, Fisher information and maximum-likelihood estimation of covariance parameters in gaussian stochastic processes, *Can. J. Stat.* **26**, 127 (1998).
- [42] J. D. Romano and N. J. Cornish, Detection methods for stochastic gravitational-wave backgrounds: a unified treatment, *Living Rev. Relativity* **20**, 2 (2017).
- [43] T. B. Littenberg, A comprehensive Bayesian approach to gravitational wave astronomy, PhD thesis, Montana State University, 2009.
- [44] S. Ghonge, K. Chatziioannou, J. A. Clark, T. Littenberg, M. Millhouse, L. Cadonati, and N. Cornish, Reconstructing gravitational wave signals from binary black hole mergers with minimal assumptions, *Phys. Rev. D* **102**, 064056 (2020).
- [45] LIGO Scientific Collaboration, LIGO Algorithm Library—LALSuite, free software (GPL), 2018.
- [46] S. Husa, S. Khan, M. Hannam, M. Pürrer, F. Ohme, X. J. Forteza, and A. Bohé, Frequency-domain gravitational waves from nonprecessing black-hole binaries. I. New numerical waveforms and anatomy of the signal, *Phys. Rev. D* **93**, 044006 (2016).
- [47] S. Khan, S. Husa, M. Hannam, F. Ohme, M. Pürrer, X. J. Forteza, and A. Bohé, Frequency-domain gravitational waves from nonprecessing black-hole binaries. II. A phenomenological model for the advanced detector era, *Phys. Rev. D* **93**, 044007 (2016).

- [48] B. P. Abbott, R. Abbott, T. D. Abbott *et al.*, Prospects for observing and localizing gravitational-wave transients with Advanced LIGO, Advanced Virgo and KAGRA, [Living Rev. Relativity](#) **21**, 3 (2018).
- [49] H.-P. Pan, C.-Y. Lin, Z. Cao, and H.-J. Yo, Accuracy of source localization for eccentric inspiraling binary mergers using a ground-based detector network, [Phys. Rev. D](#) **100**, 124003 (2019).
- [50] R. Essick, S. Vitale, E. Katsavounidis, G. Vedovato, and S. Klimentko, Localization of short duration gravitational-wave transients with the early Advanced LIGO and Virgo detectors, [Astrophys. J.](#) **800**, 81 (2015).